Icarus 357 (2021) 114282

Contents lists available at ScienceDirect

Icarus

journal homepage: www.elsevier.com/locate/icarus

Research paper

Boulder sizes and shapes on asteroids: A comparative study of Eros, Itokawa and Ryugu

Tatsuhiro Michikami [a,*], Axel Hagermann [b]

[a] Faculty of Engineering, Kindai University, Hiroshima Campus, 1 Takaya Umenobe, Higashi-Hiroshima, Hiroshima 739-2116, Japan
[b] Luleå University of Technology, Space Campus, 981 28 Kiruna, Sweden

ARTICLE INFO

Keywords:
Asteroids
Surfaces
Asteroid Eros
Asteroid Itokawa
Asteroid Ryugu
Regoliths

ABSTRACT

In order to understand the geological evolution of asteroids Eros, Itokawa and Ryugu and their collisional history, previous studies investigated boulder size distributions on their surfaces. However, quantitative comparison of these size distributions is hampered by numerous differences between these studies regarding the definition of a boulder's size, measuring technique and the fitting method to determine the power-index of the boulder size distributions. We provide a consistent and coherent model of boulder size distributions by remeasuring the boulders on the entire surfaces of Eros and Itokawa using the Small Body Mapping Tool (SBMT) and combining our observations with the Ryugu data of Michikami et al. (2019). We derived power-indices of the boulder size distributions of -3.25 ± 0.14 for Eros, -3.05 ± 0.14 for Itokawa and -2.65 ± 0.05 for Ryugu. The asteroid with the highest number density of boulders ≥ 5 m turns out to be Ryugu, not Itokawa, as suggested by an earlier study. We show that the appearance of the boulders tends towards more elongated shapes as the size of an asteroid decreases, which can be explained by differences in asteroid gravity and boulder friction angles. Our quantitative observational results indicate that boulder migration preferentially affects smaller boulders, and tends to occur on larger asteroids.

1. Introduction

The surfaces of most asteroids visited by spacecraft are characterized by numerous boulders. To date, detailed global observations of four asteroids encountered by spacecraft have been conducted: Eros (34 × 11 × 11 km; Veverka et al., 2000), explored by the NEAR spacecraft; Itokawa (0.535 × 0.294 × 0.209 km; Fujiwara et al., 2006), explored by the Hayabusa spacecraft; Ryugu (1.04 × 1.02 × 0.88 km; Watanabe et al., 2019), explored by Hayabusa2; and Bennu (0.565 × 0.536 × 0.498 km; Lauretta et al., 2019) explored by OSIRIS-REx. The detailed observations by these missions enables us to make a quantitative comparisons of boulders on all of these asteroids with their different gravities. However, a quantitative comparison of the respective boulder size distributions is hampered by different analysis methods being used in previous studies. In this study, we revisit the detailed imaging data of asteroids Eros and Itokawa and analyze their boulder sizes and shapes with a common and consistent method, as used by Michikami et al. (2019) for asteroid Ryugu.

1.1. Motivation

The motivation of this study is to understand the formation and migration of boulders on the surfaces of asteroids by comparing quantitatively the boulder size and shape distributions on the three asteroids Eros, Itokawa and Ryugu with their different gravities. In other words, we deduce the influence of gravity on the formation and migration of boulders from a quantitative comparison of the asteroids' boulder size and shape distributions.

In this study, we do not consider the boulder data on Bennu because the complete data base of global boulder distributions down to sizes as small as a few meters has not yet been published at the time of writing, although preliminary measurements of boulders on Bennu have been made by several authors (e.g. Walsh et al., 2019; Pajola et al., 2019; Schwartz et al., 2019).

1.1.1. Boulder size distributions

The power-index of boulder size distribution reflects, to a certain extent, the degree of fragmentation during the formation of an asteroid. In general, a power-index steeper than −2 is indicative of very

* Corresponding author.
E-mail address: michikami@hiro.kindai.ac.jp (T. Michikami).

https://doi.org/10.1016/j.icarus.2020.114282
Received 29 June 2020; Received in revised form 16 December 2020; Accepted 18 December 2020
Available online 24 December 2020

fragmented material, and a steeper index is further indicative of a greater degree of fragmentation (Hartmann, 1969; Thomas et al., 2001). After the formation of an asteroid, the migration of boulders, cobbles and pebbles will occur on the asteroid due to the seismic shaking produced by recurrent impacts (Miyamoto et al., 2007). The ratio of boulders migrating may be related to the global and local gravity of the asteroid. For local regions of each asteroid, it is possible that there is a relocation of boulders, with small boulders moving towards low potential, high surface gravity, regions (e.g. Tancredi et al., 2015). In this case, the boulder size distributions in different local regions may differ depending on the gravity in each region. Thus, a quantitative comparison of their respective boulder size distributions on both global and regional scales will provide important evidence to interpret the formation and migration of boulders on the three asteroids Eros, Itokawa and Ryugu with their different gravity regimes.

According to Tancredi et al. (2015) and Grott et al. (2020), the distribution of boulders observed on an asteroid's surface reflects the distribution in the asteroid interior below them. Thus, as the first step to understand the correlation between gravity and the boulder sizes and shapes, we investigate and discuss global data for each asteroid to begin with. In the penultimate section of this paper we then turn to regional data for each asteroid.

1.1.2. Boulder shape distributions

It is likely that the boulder shape distribution on an asteroid's surface captures information related to the migration of the boulders. Their shapes are mostly elongated and are considered to be similar to those of laboratory impact fragments (Michikami et al., 2019), whose shapes have been studied extensively (e.g. Fujiwara et al., 1978; Nakamura et al., 2008; Michikami et al., 2010; Michikami et al., 2016). Shapes of these fragments are generally defined by the maximum dimensions of the fragments in three mutually orthogonal planes ($a \geq b \geq c$). According to Michikami et al. (2016), the mean b/a ratios of the fragments are almost constant and independent of experimental conditions such as degree of fragmentation, target shape, composition and strength.

As mentioned above, according to Miyamoto et al. (2007), smaller boulders (gravel) were redistributed after their accumulation by global vibrations (seismic shaking) caused by repeated impacts. This is because the smaller boulders have higher mobility due to their lower friction angle. It is obvious that the migration of the boulders would affect their orientation.

If the actual shape distribution of the boulders on any asteroid is indeed similar to laboratory impact fragments, as pointed out above (we will discuss this in Section 6), the apparent a and b axes of the boulders on the surface (hereafter referred to as a' and b') provide information related to the orientation of the boulders. For instance, if the mean b'/a' ratio of the boulders is much smaller than the mean b/a in laboratory impact fragments, this suggests that most c axes are not perpendicular to the asteroid surface and most boulders are not 'lying flat' on the surface (i.e. mostly, $b' = c$ on the assumption of $a = a'$). According to Michikami et al. (2019), the orientations of the a axes of most boulders on Itokawa and Ryugu were observed to be parallel to the asteroid surface. Only the orientations of b and/or c axes would be somewhat random. Therefore, on the hypothesis that the actual boulder shapes are similar to laboratory impact fragments, a quantitative comparison of boulder shape distributions is helpful to find a clue to the orientation and migration of the boulders.

1.2. Previous studies and issues in terms of boulder sizes and shapes

Boulder size distributions on the three asteroids have been investigated by several researchers. However, when comparing their boulder size distributions, (i) the definition of a boulder size, (ii) the measuring technique and (iii) the fitting method to determine the value of the exponent in the power-law size distribution, differ from author to author. It is therefore difficult to compare their boulder size distributions quantitatively. The details are as follows.

(i) Boulder size definition

In previous studies, there have been several categories of defining a boulder's size. The first definition is used by, e.g., Saito et al. (2006) and Sugita et al. (2019), who chose the long axis (a') to define boulder size on Itokawa and Ryugu, respectively. The second definition involves measuring the line coordinates for a minimum of six points around the boulder periphery and converting this into average diameters (mean horizontal dimensions), as applied to Eros by Thomas et al. (2001) and Chapman et al. (2002). The third one approximates the outline of boulders as ellipses whose long (a') and short (b') axes are measured. For example, in Michikami et al. (2008) for Itokawa and Michikami et al. (2019) for Ryugu, the mean diameter is defined as the arithmetic mean of these two axes. Tancredi et al. (2015) define the mean diameter as the geometric mean of these two axes for Itokawa. The fourth definition approximates the boulder shape as an ellipsoid, and boulder size is defined as the diameter of a sphere whose volume is equivalent to that of the ellipsoid. For instance, Mazrouei et al. (2014) measured the horizontal long and short axes of boulders on Itokawa and assumed the height (vertical dimension) of a boulder to be equal to its horizontal short axis.

In laboratory impact experiments, the sizes of fragments are typically presented in terms of their mass. As pointed out by Mazrouei et al. (2014), studies evaluating boulder sizes on asteroids could be more meaningfully compared to experiments if boulders could also be analyzed in terms of their mass and volume, although the heights are difficult to determine. Therefore, it is necessary to find a robust definition of boulder size that is representative of mass or volume of the boulder even when the heights cannot be measured.

(ii) Measuring technique

The two most commonly used measuring tools for surface boulder mapping are SAOImage DS9 and the Small Body Mapping Tool (SBMT; Ernst et al., 2018). DS9 is an astronomical or planetary imaging and data visualization application. It was used, e.g., by Saito et al. (2006), Michikami et al. (2008) and Tancredi et al. (2015) for measuring the boulders on Itokawa. However, one of the uncertainties introduced by using DS9 is related to map projection. There is a possibility that some boulder sizes cannot be measured precisely, especially when a boulder on the surface is observed from an oblique camera angle, resulting in smaller apparent sizes due to map projection issues. Tancredi et al. (2015) corrected this effect by applying a correction factor that depends on the cosine of the emission angle.

SBMT, on the other hand, is a more powerful tool to measure boulder sizes because it provides the boulder data on the asteroid's shape model and thus an appropriate map projection for measuring boulder sizes accurately is available. SBMT includes parametric information for each image and region such as location, emission angle, elevation, gravitational acceleration and potential, image scale etc. Consequently, SBMT is ultimately a more suitable tool for measuring and mapping boulders. SBMT was not yet available at the time of earlier studies measuring boulders on Eros. Therefore, remeasurement of the sizes and shapes of boulders on Eros is necessary in order to quantitatively compare the boulders on Eros, Itokawa and Ryugu.

(iii) Fitting method

In general, boulder size distributions are expressed using power laws, with the power-indices of boulder size distributions often estimated by least-squares fits in previous studies (e.g. Michikami et al., 2008; Mazrouei et al., 2014). However, this method is subject to systematic errors that can lead to an underestimation of uncertainties and/or a biasing of the power-index (Clauset et al.,

2009; DeSouza et al., 2015). The power-law fitting procedure proposed by Clauset et al. (2009) is currently considered to be suitable for a boulder dataset, i.e. the power-index of a boulder size distribution is obtained combining a maximum-likelihood fitting method with goodness-of-fit tests based on the Kolmogorov-Smirnov statistic and likelihood ratios. There is a difference in power-indices of the power laws derived using a least-squares fit and the maximum likelihood method described by Clauset et al. (2009) even if identical data is used. For instance, in the data of Mazrouei et al. (2014), the power-indices of the boulder size distribution on Itokawa are -3.3 ± 0.1 using least-squares fit and -3.52 ± 0.20 using Clauset et al.'s (2009) fitting method (Michikami et al., 2019). Using Clauset et al.'s (2009) method, DeSouza et al. (2015), Tancredi et al. (2015) and Michikami et al. (2019) have estimated the power-indices of the cumulative boulder size distributions on Itokawa and Ryugu. On Eros, the power-index of the boulder size distribution was not estimated using this fitting method.

In addition to boulder size definition, measuring technique and fitting method, observer bias is highly probable, i.e. it is likely that the each observer derives a different size measurement of the same boulder because individual observers trace the outline of the boulder periphery differently. According to Michikami et al. (2008), the error caused by the scatter between the measurements performed by three different individuals, is within a tolerance of 15% for the size. To avoid this, boulders on Eros and Itokawa were measured by only one individual (T. Michikami) using SBMT in this study. For the boulders on Ryugu, we adopt the data of Michikami et al. (2019), with measurements taken by T. Michikami alone.

Finally, some observers identify boulders where others do not. We define a boulder as an isolated positive relief feature with a size larger than 256 mm on the surfaces of the asteroids. Some appear as piles of gravel or a part of a geologic feature such as protruding bedrocks, raised crater rims, or intersecting crater walls. We provide more details on the definition of a boulder and data handling in SBMT, in Sections 3 and 4.

1.3. Outline of this paper

In Section 2, we evaluate a suitable definition of boulder size as the representation of a boulder's volume. We use fragments of laboratory impact experiments into basalts (Michikami et al., 2016) as analogues and investigate the relationship between the fragments' sizes in terms of long, short axes and/or heights of the fragments, and the fragment volume based on the mass of the fragments. We consider this a suitable proxy for the relationship between boulders' sizes and their volumes because the shapes of boulders on asteroids are similar to laboratory impact fragments, as has been pointed out. For instance, Nakamura et al. (2008) found that the shapes of boulders on Itokawa are similar to laboratory impact experiment fragments despite several orders of magnitude difference in size between the two.

In Sections 3 and 4, we describe boulder size and shape measurements on Eros and Itokawa using SBMT. On Eros, there are no data for the boulder shapes on the entire surface. Thus, the boulder shapes data obtained from the measurements in SBMT are useful for understanding the formation and migration of the boulders on Eros. On Itokawa, Mazrouei et al. (2014) have already investigated the sizes and shapes of the boulders using SBMT. However, the number of boulders differs considerably from the earlier study by Michikami et al. (2008). We investigate the cause of the difference by remeasuring the boulders on Itokawa using SBMT rather than DS9.

Using these boulder mapping data, we quantitatively compare global boulder size and shape distributions on Eros, Itokawa and Ryugu (Section 5). In Section 6, we focus on local regions for each of the three asteroids, and discuss the correlation between gravity and boulder sizes and shapes from global and local surface data, which helps us infer the most likely formation and boulder migration mechanisms on the three asteroids. Finally, we present our conclusions in Section 7.

2. Shapes, sizes and volumes of rocks

2.1. Five categories for the definition of boulder size

As mentioned above, the shapes of fragments in laboratory impact experiments have often been characterized by axes a, b and c, these being the maximum dimensions of the fragment in three mutually orthogonal planes ($a \geq b \geq c$). When counting boulders on asteroids using images of an asteroid's surface, three-dimensional information about the orientations of boulders is often lacking. Therefore, rock dimensions measured from spacecraft need to be treated as apparent dimensions a', b', c' and are denoted with an apostrophe. In most cases only the a' and b' axes of the boulders can be estimated because, frequently, boulder height information is missing entirely. In general, the relation between these dimensions is considered to be: $a \geq a' \geq b$; $b \geq b' \geq c$. Laboratory impact fragments, on the other hand, are accessible from all directions and their actual dimensions a, b, c can be measured directly.

The above definitions of a boulder size can be classified into four categories, as there are

(1) the long axis of the horizontal dimension, a;
(2) the mean diameter of the long and short axes of the horizontal dimension as the arithmetic mean of these two axes, $\frac{a+b}{2}$;
(3) assuming the vertical axis, c to be equal to the horizontal short axis, b, the mean diameter of a sphere whose volume is equivalent to that of an ellipsoid, $\left(ab^2\right)^{\frac{1}{3}}$; or,
(4) the mean diameter of the long and short axes of the horizontal dimension as the geometric mean of these two axes, $(ab)^{\frac{1}{2}}$.

Of course, if the c axis of a boulder is measured, the volume approximated by the ellipsoid will be close to the real volume of the boulder. In this study, in addition to the above four categories, one more category is considered,

(5) the mean diameter of a sphere whose volume is equivalent to that of an ellipsoid, $(abc)^{\frac{1}{3}}$.

For the sake of simplicity, we will abbreviate a, $\frac{a+b}{2}$, $\left(ab^2\right)^{\frac{1}{3}}$, $(ab)^{\frac{1}{2}}$ and $(abc)^{\frac{1}{3}}$ as D_1, D_2, D_3, D_4 and D_5, respectively. The relationships between fragments' sizes defined by $D_1 - D_5$ and their volumes are investigated using the fragment data of laboratory impact experiments into basalt. A short description of these experiments is given in the appendix. Experimental conditions and results are summarized in Table 1.

2.2. Relationship between a fragment's size and its volume

We start our investigation into a robust definition of boulder size that is representative of mass or volume of the boulder by selecting shot s2126 from Michikami et al. (2016) because this shot resulted in 1659 fragments with $b \geq 4$ mm, the largest number in the experimental campaign. The impact velocity for this shot was 6.99 km/s and the target had a side length of 7.5 cm. The target was completely shattered into small fragments.

Instead of the real volume of the fragments, in this study, we adopt the sphere-equivalent diameter, D_s $\left(= \left(\frac{6m}{\rho\pi}\right)^{\frac{1}{3}}\right)$, which is calculated from the fragment mass, m with a density of ρ=3000 kg/m^3. Fig. 1 shows the sphere-equivalent diameter, D_s vs. the fragment sizes $D_1 - D_5$ with the correlation coefficient R. For D_1,R is slightly smaller than for the other

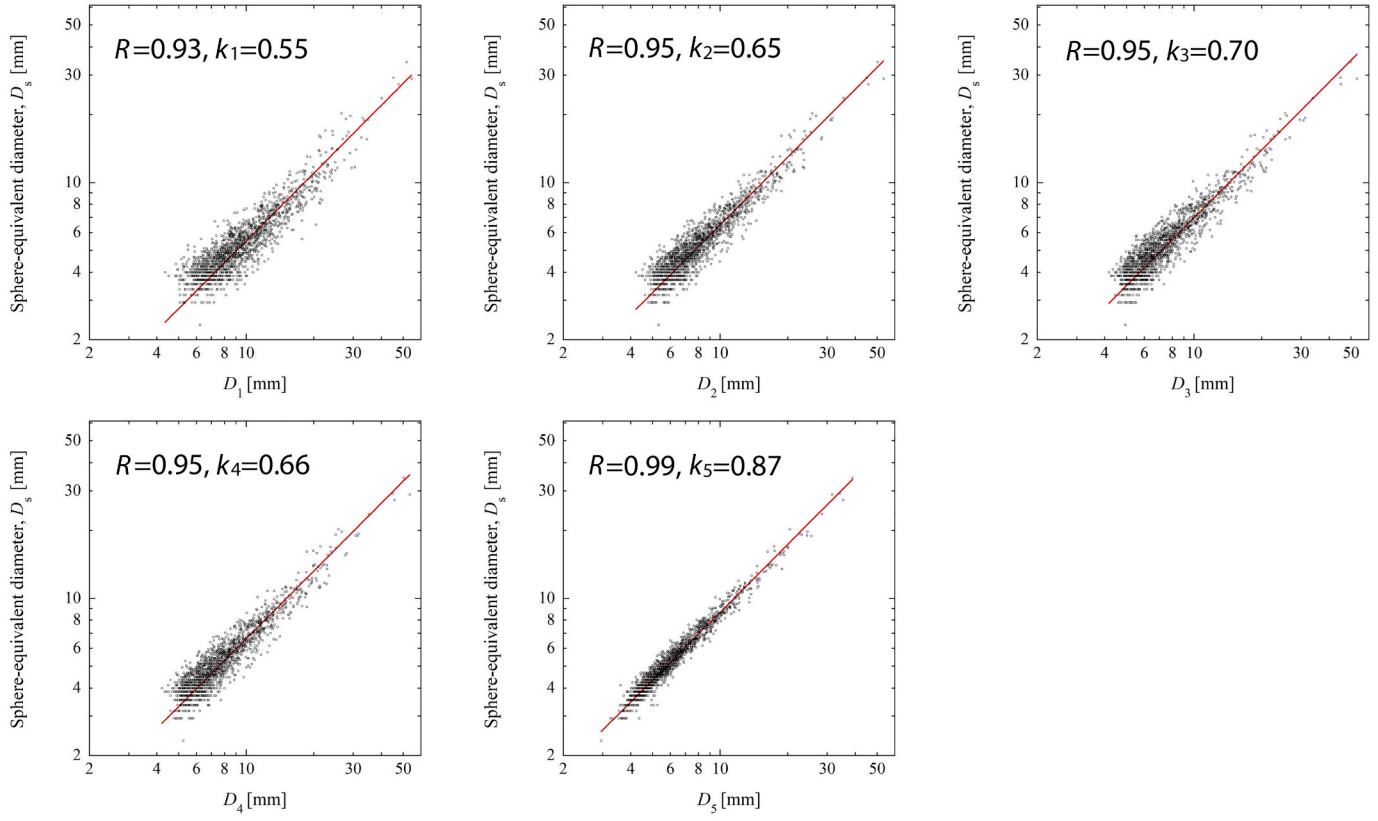

Fig. 1. Diagrams for the sphere-equivalent diameter, D_s vs. fragment sizes D_1 – D_5, where D_1=a, D_2=$\frac{a+b}{2}$, D_3=$\left(ab^2\right)^{\frac{1}{3}}$, D_4=$(ab)^{\frac{1}{2}}$ and D_5=$(abc)^{\frac{1}{3}}$, with a, b and c the maximum dimensions of the fragment in three mutually orthogonal planes ($a \geq b \geq c$). The correlation coefficients R are listed. When the sphere-equivalent diameter, D_s, is expressed as k_xD_x (where x = 1,2,3,4,5), the value of k_x is calculated using least-squares and is listed for each fragment size. These fragments are obtained from shot s2126 in Michikami et al. (2016).

size definitions, which may be caused by having only one direction of measurement of the fragments. However, in all cases correlation is good, especially for D_5 as a matter of course.

The real volume of a fragment can be expressed as $\frac{\pi}{6}D_s^3$, or simply $\frac{\pi}{6}D_x^3$ (with x = 1,2,3,4,5) if fragment size D_x equals the sphere-equivalent diameter D_s. However, the sphere-equivalent diameter of the fragment, D_s, is smaller than the fragment's size D_x in all cases, so that the real volume (expressed as $\frac{\pi}{6}D_s^3$) is less than the calculated volume ($\frac{\pi}{6}D_x^3$). This can be remedied by introducing a correction factor, k_x, to express the sphere-equivalent diameter, D_s, as k_xD_x. k_x can be found using the least-squares method and always has to be less than 1 because the real volume of any fragment is less than the ellipsoidal volume approximated by its axes a, b and c.

In previous studies, the volumes of individual boulders were calculated from the ellipsoidal volume, $\frac{\pi}{6}abc_h$, where the value of c_h is subject to observer bias. For an example, Mazrouei et al. (2014) have assumed values of $c_h = b$. In this case, $c_h > c$ because $a \geq b \geq c$ and, as a consequence, the volumes of individual boulders on asteroids have been overestimated in previous studies. Therefore, it is necessary to re-estimate the volume of boulders using the correction factor k_x.

Next, we investigate the power-index of the cumulative fragment size distribution by combining a maximum-likelihood fitting method with goodness-of-fit tests based on the Kolmogorov-Smirnov statistic and likelihood ratios (Clauset et al., 2009; DeSouza et al., 2015; Tancredi et al., 2015). Fig. 2 shows the cumulative fragment size distributions from shot s2126 for each fragment size definition. The red line indicates the best fit power law for the each data set corresponding to the respective D_x.

In contrast to the R values, the calculated power-indices of the cumulative size distributions show some scatter, ranging from 2.81 to 3.68. The power-index for the sphere-equivalent diameter, D_s is 3.68, and is greater than for fragment sizes D_1 – D_5. For fragment size D_5, the power-index (3.49) is closest to the value for D_s. We can therefore conclude that D_5 reflects the real volume of the fragments better than the other fragment size definitions D_1 – D_4. However, when counting boulders on an asteroid, the c axis of a boulder is notoriously difficult to determine. The power-index (3.42) for fragment size D_2 is the next-best approximation of D_s and determining D_2 does not require knowledge of c. In shot s2126, the total volume of fragments calculated by using the fragment size k_2D_2 with k_2=0.65 is 322 cm^3, which is similar to the volume of the real fragments measured (315 cm^3). Thus, we can consider the fragment size definition D_2 to be good proxy for the real volume of boulders – only bettered by size definition D_5.

In a catastrophic disruption like shot s2126, the axial ratios of fragments are distributed around mean values of b/a ~0.7 and c/a ~0.5, i.e. corresponding to a simple a: b: c proportion of 2: $\sqrt{2}$: 1 (Fujiwara et al., 1978; Capaccioni et al., 1984, 1986; Durda et al., 2015; Michikami et al., 2016). However, in general, the shape distribution of the fragments depends on the degree of fragmentation of the target (Michikami et al., 2016). Fragments from impact cratering tend to have flatter shapes, i.e. their b/a and c/a are ~0.7 and ~0.2, respectively (Michikami et al., 2016). The mean c/a ratio decreases with decreasing specific energy, Q, which is defined as the kinetic energy of the projectile per unit target mass (Michikami et al., 2016). Or, put more simply, the lower the impact specific energy, the flatter the fragments.

In order to examine that the fragment size D_2 is a good enough approximation for the real volume of the boulders even when the mean c/a ratio is small, we selected five more shots, s2129, s2130, s2131, s2570 and s2572 from the data of Michikami et al. (2016). The reason for this choice is their range of impact velocities, which were

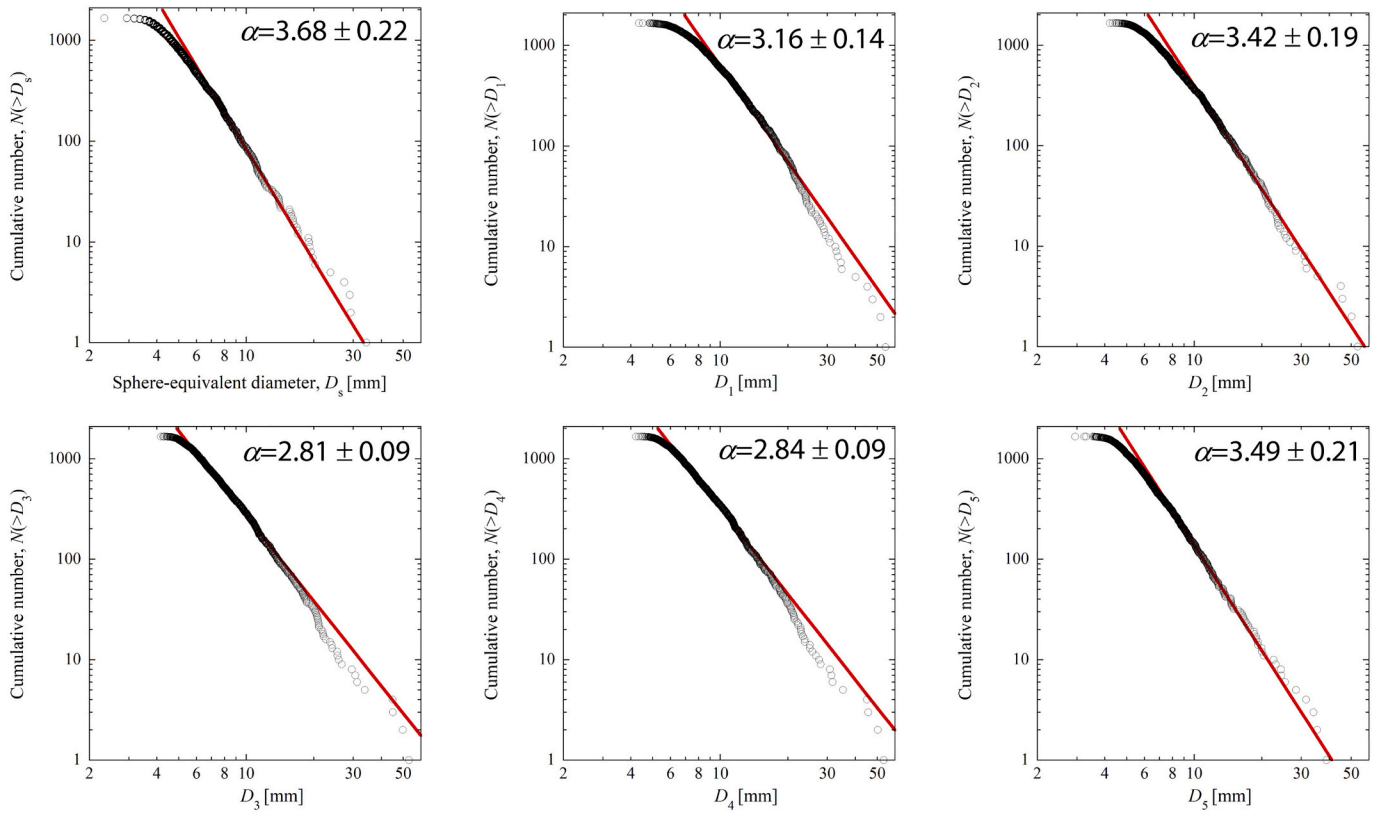

Fig. 2. Cumulative fragment size distributions for sphere-equivalent diameter, D_s and fragment sizes $D_1 - D_5$ for the data in Fig. 1. The value of the power-index α to the upper right of each graph is obtained by combining a maximum-likelihood fitting method with goodness-of-fit tests based on the Kolmogorov-Smirnov statistic and likelihood ratios (Clauset et al., 2009; Tancredi et al., 2015). The red line corresponds to the best fit power law for each data set. (For interpretation of the references to colour in this figure legend, the reader is referred to the web version of this article.)

approximately maintained (~5 km/s, except for s2572) while the target sizes varied between 5 cm and 15 cm side length. Target properties and experimental results are summarized in Table. 1, which gives the k_2 values for all fragment sizes in every shot. These size distributions refer to Fig. 7 in Michikami et al. (2016).

Fig. 3 shows the relationship between the mean c/a ratios and the power-index of the size distributions of laboratory impact fragments, in terms of the sphere-equivalent diameter, D_s, and fragment sizes, $D_1 - D_5$. From Fig. 3, it is difficult to determine the next-best proxy for D_s. However, with the exception of D_5, we consider fragment size definition D_2 to be a suitable proxy for D_s, because the mean c/a ratios of the fragments in a catastrophic disruption are greater than 0.4 and the power-indices of the fragment size definition D_2 are close to those of D_s. In addition, even when the mean c/a ratios are less than 0.4, the power-indices for D_2 are not so different from those of D_s. As a fragment size proxy, D_2 does not fare much worse than D_5, although it requires less information than the latter. In conclusion, and for want of a substantially more accurate and practical alternative, we choose fragment size D_2 as a suitable proxy for the real volume of boulders even when the mean b/a and c/a ratios of the boulders deviate from of 0.7 and 0.5, respectively.

3. Boulders on asteroid Eros

Approximating the outlines of boulders as ellipses, the apparent long and short axes of boulders on Eros are measured using SBMT. $D_2 = \frac{a'+b'}{2}$ is adopted as the definition of boulder size hereafter, i.e. the mean horizontal dimension of a boulder is defined as the arithmetic mean of the apparent long and short axes.

Measuring boulders on Eros using SBMT, we adopted the high resolution mosaic map from NASA's PDS ("https://sbnarchive.psi.edu/pds3/multi_mission/MULTI_SA_MULTI_6_STOOKMAPS_V3_0/document/433eros/eros_cyl_near.jpg"). Only near the equator at 200° and 310°E longitude, we adopted another set of images because the distortions caused by the irregular shape of Eros are particularly apparent in these areas. Only a small number of boulders is obtained from these and

Table 1
Target properties and experimental results from the data of Michikami et al. (2016). M_t, M_l and Q are initial target mass, largest fragment mass and specific energy, respectively. The mass and shapes of the fragments with $b \geq 4$ mm are measured. In s2570 and s2572, the fragment count and the mean values of b/a and c/a do not contain the largest fragment whose mass is roughly the same as the initial target mass. The definition of k_2 is given in the text.

Shot number	Dimension [cm]	M_t [g]	Impact features			Fragments			k_2
			Velocity [km/s]	Q [J/kg]	M_l/M_t	Mean value of b/a	Mean value of c/a	Counted number ($b \geq 4$ mm)	
s2126	7.5 × 7.5 × 7.5	1240.4	6.99	4280	0.051	0.71	0.41	1659	0.65
s2129	5 × 5 × 5	360.9	5.32	8540	0.018	0.74	0.45	756	0.67
s2130	7.5 × 7.5 × 7.5	1227.1	5.27	2470	0.088	0.71	0.41	1194	0.65
s2131	10 × 10 × 10	2948.9	5.32	1050	0.211	0.71	0.38	686	0.65
s2570	15 × 15 × 15	10031.0	5.01	270	0.944	0.71	0.26	118	0.59
s2572	15 × 15 × 15	10058.0	3.72	150	0.997	0.66	0.17	23	0.47

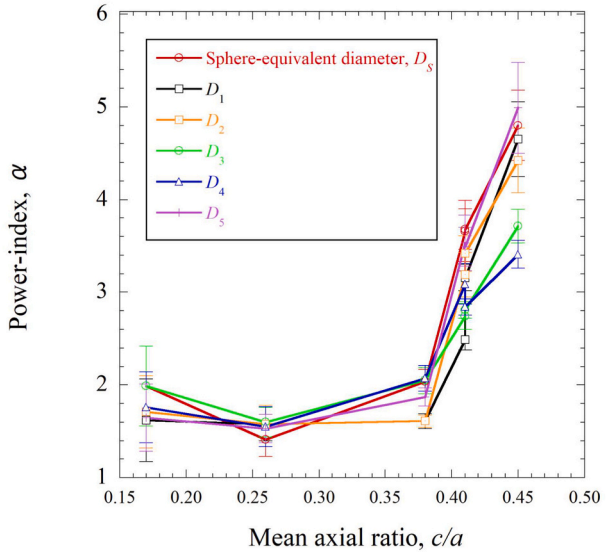

Fig. 3. Relationship between mean c/a ratio and power-index of the size distributions for the sphere-equivalent diameter, D_s and the fragment sizes, $D_1 - D_5$ of laboratory impact fragments obtained from shots s2126, s2129, s2130, s2131, s2570 and s2572 in Michikami et al. (2016). In s2570 and s2572, the fragment count, the power-induces and the mean values of b/a and c/a do not contain the largest fragment whose mass is roughly the same as the initial target mass. Even if the data of s2570 and s2572 processed including the largest fragments, almost all values of the power-induces fall within the error range shown (even when a data has the power-index of the outside of the error range, for the very few exceptions falling outside the error range the excess from the error range is very small).

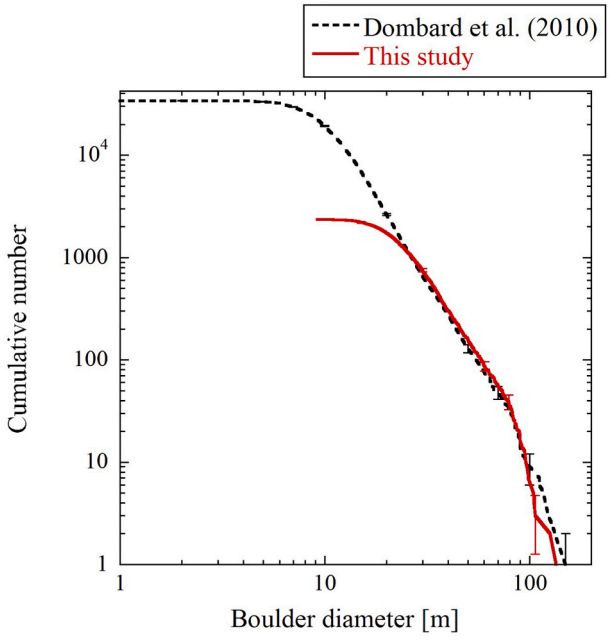

Fig. 4. Global, cumulative boulder size distribution on Eros. The black dashed line shows the data of Dombard et al. (2010), who measured 33,939 boulders. The red solid line indicates the data of this study measuring 2346 boulders larger than 9 m. Vertical error bars are the roots of the counts and are given only for a few points to keep the figure legible. The power-indices of the size distributions in the data of Dombard et al. (2010) and this study are -3.28 ± 0.15 and -3.25 ± 0.14, respectively. (For interpretation of the references to colour in this figure legend, the reader is referred to the web version of this article.)

almost all boulders are measured using the mosaic map.

As pointed out by Chapman et al. (2002), most boulders on Eros are too small for their shapes to be well resolved in even the highest resolution images. In this study, we focus on those boulders that are larger than 30 m because of limited image resolution. Boulders larger than 30 m are mapped on a global scale and are measured on the shape model of Eros (NEAR-A-MSI-5-EROSSHAPE-V1.0) produced by R.W. Gaskell in 2008 ("https://sbn.psi.edu/pds/resource/erosshape.html"). The boulder size and space distributions in this study are compared to the data of Thomas et al. (2001) and Dombard et al. (2010).

3.1. Boulder size distribution

Fig. 4 compares the cumulative boulder size distribution across the entire surface of Eros from Dombard et al. (2010) with this study. Dombard et al. (2010) expanded the data of Thomas et al. (2001) and constructed a database of all boulders on Eros larger than 15 m, and in places down to < 0.1 m in size. They measured 33,939 boulders on Eros. In this study, more than 2300 boulders larger than 9 m in diameter were measured and a total of ~750 boulders larger than 30 m were observed over the entire surface area of 1129.6 km^2. The rollover for boulders smaller than ~ 30 m is a sampling bias introduced by the resolution of the images. At diameters $\geq$ 30 m, the boulder size distribution in this study is similar to Dombard et al. (2010).

We compute the power-index of the cumulative boulder size distribution on Eros by combining a maximum-likelihood fitting method with goodness-of-fit tests based on the Kolmogorov-Smirnov statistic and likelihood ratios. The resulting power-indices for the size distributions in Dombard et al. (2010) and this study are similar, at -3.28 ± 0.15 and -3.25 ± 0.14, respectively.

A minor difference between Dombard et al. (2010) and our observation is the diameter of the largest boulder which, in our observations, is 135 m, slightly smaller than the 150 m given by Dombard et al. (2010) and Thomas et al. (2001). Moreover, our study finds 100 more boulders larger than 30 m than Dombard et al. (2010). This may be due to observer bias because the tracing outline of the boulder periphery depends somewhat on the individual observer. However, it can be shown that the differences are negligible from a statistical point of view: for boulders larger than 30 m, the p-value of the Wilcoxon rank sum test between the data of Dombard et al. (2010) and this study is 0.14, suggesting a 95% confidence level that the difference is not statistically significant. The similarity between the measuring techniques can be explained by the fact that Dombard et al. (2010) – as well as Thomas et al. (2001) and Chapman et al. (2002) also determined the boulder size by projection onto the shape model.

3.2. Boulder spatial distribution

In line with Thomas et al. (2001), we find that most boulders are located near Shoemaker crater and boulders outside Shoemaker crater are concentrated near the equator (Fig. 5). To quantitatively illustrate this, the histograms of distributions of boulders as a function of longitude and latitude are shown in Fig. 6. The boulders in a given longitude and latitude bin are normalized by the corresponding surface area of Eros in the respective bin. The shapes of the histograms for the data of Thomas et al. (2001) and this study are similar in that the longitude distribution in Fig. 6a exhibits a peak at longitude 20°-60°E, which corresponds to the area of Shoemaker crater, and the latitude distribution in Fig. 6b shows a peak near the equator. As an exception, at latitude −90° to −80°, the observed boulder exists only in the data of Thomas et al. (2001). This is because latitude −90° to −80° denotes a very small surface area in which there is only one boulder. The p-values of a chi-squared goodness-of-fit test in longitude and latitude are 0.98 and 0.97, respectively, suggesting a 95% confidence level that the difference is not statistically significant. Thus, for diameters $\geq$ 30 m, the spatial distributions of the boulders observed by Thomas et al. (2001) and this

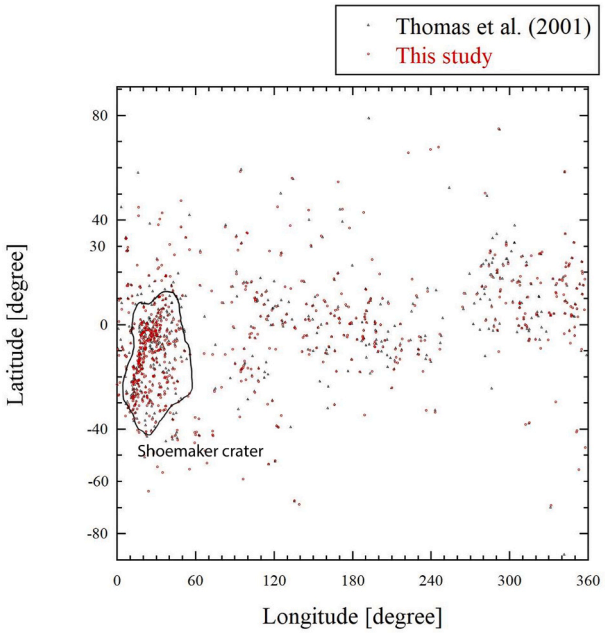

Fig. 5. Spatial distribution of boulders larger than 30 m on Eros. The map is a simple cylindrical projection with the Shoemaker crater outlined. The black and red points show the data of Thomas et al. (2001) and this study, respectively. The apparent discrepancy in the individual locations of small boulders around 30 m is brought about by the difference between Thomas et al.'s and our measured sizes. (For interpretation of the references to colour in this figure legend, the reader is referred to the web version of this article.)

study are similar. In conclusion, our observational results for boulder size and spatial distributions show that our data are highly reliable.

3.3. Boulder shape distribution

We investigate the apparent b/a (b'/a') ratios of all boulders larger than 30 m over the entire surface of Eros. Note that Michikami et al. (2010) also investigated the b'/a' ratios of some boulders on Eros. However, their preliminary measurements were only made in a few arbitrarily selected locations rather than over the entire surface.

Fig. 7 shows the histogram of the b'/a' ratios of all boulders with sizes from 30 m to 135 m on Eros. The mean b'/a' ratio is 0.72. This is similar to the ratios of laboratory impact fragments, which lie in the range 0.70–0.74 (Fujiwara et al., 1978; Capaccioni et al., 1984, 1986; Michikami et al., 2016; Michikami et al., 2018). In addition, the shape of the histogram of Fig. 7 also resembles that for laboratory impact fragments. For instance, there are relatively few boulders with $b'/a' < 0.4$ on Eros, a result also observed for laboratory impact fragments.

According to Michikami et al. (2008 and 2019), on asteroids Itokawa and Ryugu there is a difference in shape between large and small boulders (which we will discuss later in more detail). We have plotted a diagram of mean b'/a' axial ratios vs. boulder sizes (Fig. 8). Fig. 8 shows

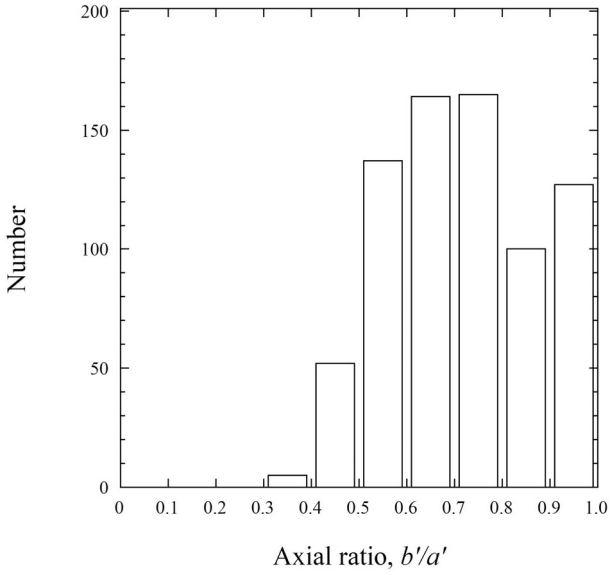

Fig. 7. Histogram of b'/a' ratios of boulders larger than 30 m across the entire surface of Eros, where a' and b' are the apparent long and short axes of the boulders. For more detail, see text.

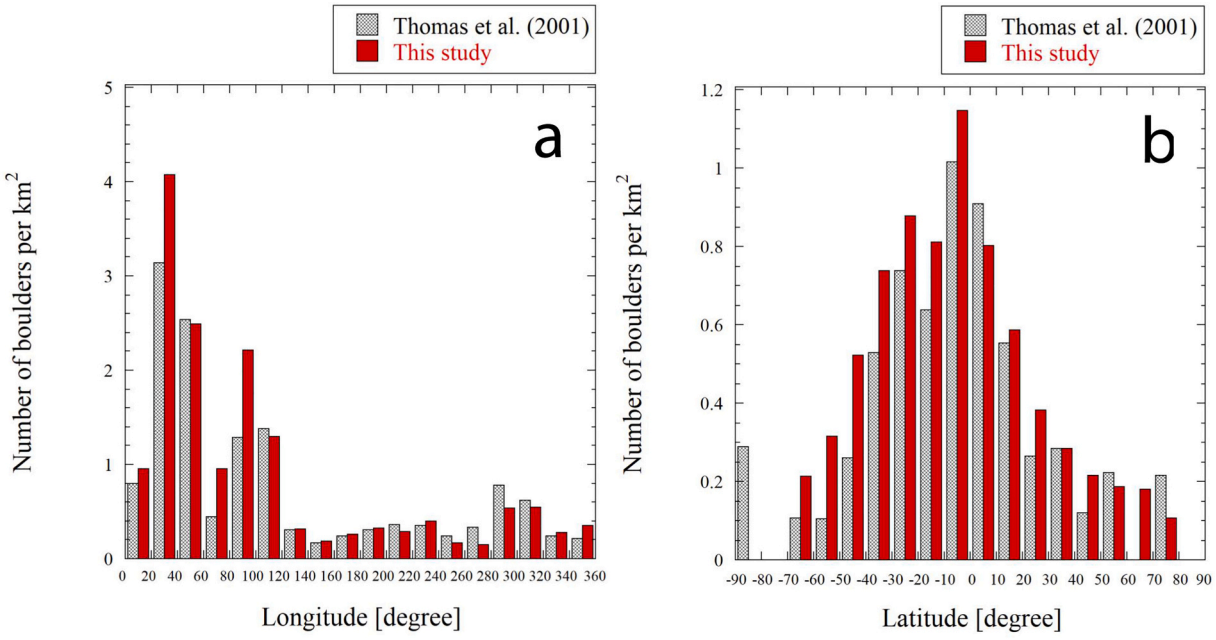

Fig. 6. Histogram of boulder surface densities for boulders larger than 30 m as a function of (a) longitude and (b) latitude on Eros.

that the mean b'/a' ratio of the boulders tends to increase slightly as the boulder diameter decreases.

4. Boulders on asteroid Itokawa

The sizes and shapes of the boulders on Itokawa are measured using the method described above. We analyze AMICA images taken by the Hayabusa spacecraft. Note that it is very important to select images with good lighting, viewing geometries and resolution. In order to investigate the sizes and shapes of the boulders accurately across the entire surface of Itokawa, measurements were conducted using twelve images with resolutions ~0.4 m/pixel acquired between 19 and 26 October 2005. As far as practicable, we restricted our measurements to boulders observed in the middle of the images so as to avoid image distortion caused by the map projection onto the shape model. The relationship between the selected images and the boulder mapping area is shown in Fig. 9.

Once again, limited image resolution leads us to focus on larger boulders – in this case the threshold is 5 m. Boulders are mapped on a global scale and are measured on R.W. Gaskell's 2008 shape model of Itokawa (HAY-A-AMICA-5-ITOKAWASHAPE-V1.0, "https://sbn.psi.edu/pds/resource/itokawashape.html"). The observational results for the boulder size and shape distributions in this study are compared to the data of Michikami et al. (2008), Mazrouei et al. (2014) and Tancredi et al. (2015).

4.1. Boulder size distribution

Nearly 1500 boulders larger than 1.6 m in diameter were measured and a total of ~490 boulders larger than 5 m were observed over the entire surface area of 0.3986 km^2. Fig. 10 shows the cumulative boulder size distributions from Michikami et al. (2008), Mazrouei et al. (2014) and this study across the entire surface of Itokawa. In this study we found slightly more boulders than Michikami et al. (2008). The difference is probably caused by a more accurate estimation of boulder size using SBMT and a more complete population of boulders, especially in high latitude areas. In other words, the difference between the data of Michikami et al. (2008) and this study stems from using SBMT rather than DS9. On the other hand, we have observed considerably fewer boulders in this study than Mazrouei et al. (2014), despite using the same tool, SBMT. For instance, we found 289 boulders larger than 6 m, only half as many as Mazrouei et al. (2014), who found 596.

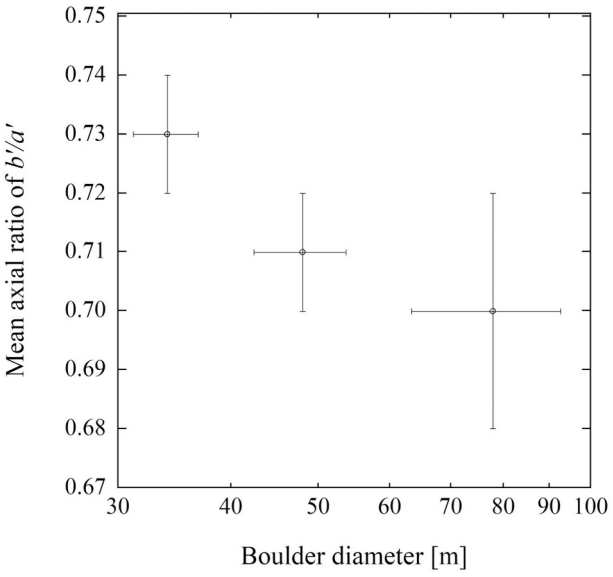

Fig. 8. Diagram of mean b'/a' ratio vs. boulder representative diameter for the size range on Eros, using the data presented in Fig. 7. The boulder representative diameter is the mean diameter of boulders in each bin. The three representative diameters for the size range are 34 m, ranging from 30 to 40 m (448 boulders), 48 m, ranging from 40 to 60 m (215 boulders), and 78 m in the range larger than 60 m (87 boulders). Standard error and standard deviation of each bin are shown as vertical and horizontal bars, respectively.

In order to investigate the discrepancy, we obtained the raw data of Mazrouei et al. (2014) and compared this study with their data. We found that the tracing outline of the boulder periphery by Mazrouei et al. (2014) is generally larger than ours. One possible explanation is that Mazrouei et al. (2014) have measured boulders from sub-optimal images whose resolution is lower than the images we selected. They used images with a resolution of <1 m/pixel, while we restricted our study to images with a resolution of ~0.4 m/pixel. From our experience, the tracing outlines of the boulder periphery on low-resolution images tend to be larger than on the high resolution images, and sometimes a cluster of boulders is mistaken for a single boulder on low-resolution images. Tendencies for both can be seen in the raw data of Mazrouei et al. (2014).

As described in Section 1.2, the size error caused by the difference between measurements performed by different observers is around 15% even if these observers use images of identical resolution. We confirmed the reliability of our measurements in a very tangible way by producing a miniature model of the asteroid surface using laboratory impact fragments and checking fragments' real and apparent sizes measured from images taken at different simulated solar angles. It should be stressed at this point, however, that what matters most for this study is not the correctness (or otherwise) of an individual observer's measurements but the consistent application of the same methodology by the same observer across three different asteroids.

Once again, we compute the power-index of the cumulative boulder size distribution on Itokawa by combining a maximum-likelihood fitting method with goodness-of-fit tests based on the Kolmogorov-Smirnov statistic and likelihood ratios as above. We find the power-indices for the data of Mazrouei et al. (2014), Michikami et al. (2008) and this study to be -3.52 ± 0.20, -3.34 ± 0.19 and -3.05 ± 0.14, respectively.

As we are now looking at three statistical populations with non-normal distributions, we use a Kruskal-Wallis test, a suitable test for confirming the difference between more than two statistical populations with non-normal distributions. The resulting p-value among these boulder size distributions is 0.36, suggesting a 95% confidence level that the difference is not statistically significant, although Mazrouei et al. (2014) and this study appear to differ in terms of the number density of boulders.

Itokawa's shape is characteristic in that it resembles a "sea otter" composed of a smaller, rather round head and a larger oval body (Fujiwara et al., 2006). The boulder size distributions on head and body are shown in Fig. 11. As one can see, the power-index (-2.62 ± 0.19) of the boulder size distribution on the head is not as steep as that (-3.44 ± 0.22) on the body. The head and body power-indices are compatible with the data of Michikami et al. (2008) and Tancredi et al. (2015), but, although the same tendency was also seen in the data of Mazrouei et al. (2014), their power-indices (head: −3.1, body:−3.6) differ somewhat from this study.

4.2. Boulder shape distribution

Using SBMT, we investigate the apparent b/a (b'/a') ratios of all boulders larger than 5 m over the entire surface of Itokawa. Mazrouei et al. (2014) did the same for boulders larger than 6 m, which is why the histograms of the b'/a' ratios of boulders larger than 6 m are shown in Fig. 12 for comparison of both studies. The histograms for both studies are similar, although the mean b'/a' ratio of the boulder larger than 6 m in this study is 0.62, slightly less than Mazrouei et al.'s value (0.65). Michikami et al. (2010) also investigated the b'/a' ratios of all boulders larger than 5 m over the entire surface of Itokawa using DS9, although they corrected the axial ratios of the boulders taking into account boulder's map projection on the surface. Both their histogram shape and

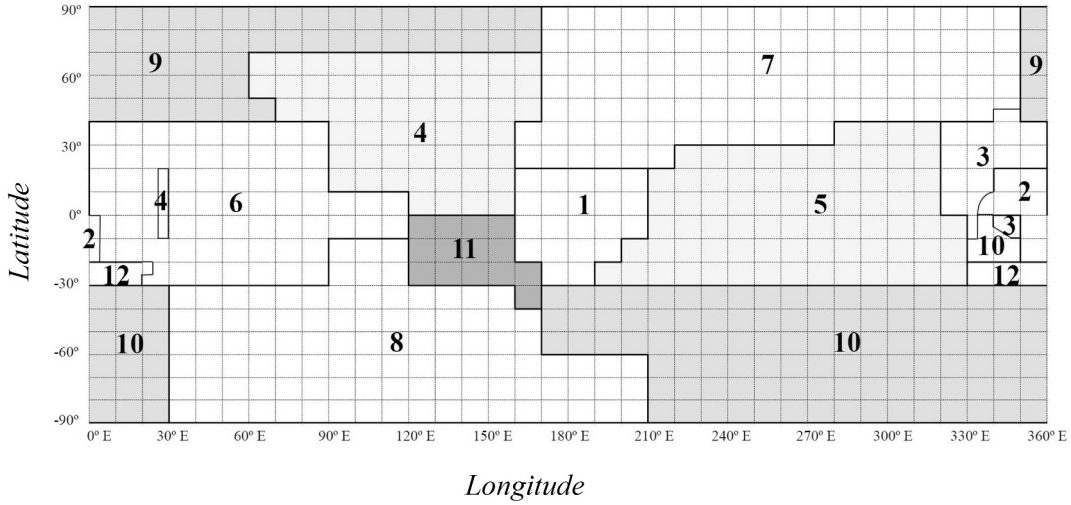

Fig. 9. Relationship between selected images (bold numbers) and boulder mapping area on Itokawa. The map is a simple cylindrical projection. Image ID's for the respective number, 1: ST2492513077, 2: ST2482160259, 3: ST2485860275, 4: ST2484352917, 5: ST2492225173, 6: ST2493031594, 7: ST2481211873, 8: ST2473604354, 9: ST2481672682, 10: ST2472657784, 11: ST2474616313, and 12: ST2472776818.

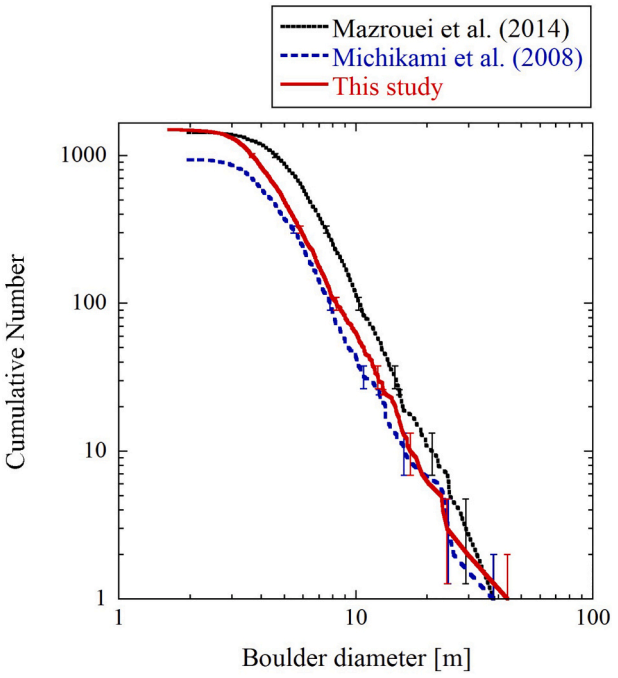

Fig. 10. Global, cumulative boulder size distributions on Itokawa. Black, blue dashed and red solid lines show the data of Mazrouei et al. (2014), Michikami et al. (2008) and this study, respectively. For the sake of legibility, vertical error bars, which represent the roots of the counts, are only given for a few points. The power-indices of the size distributions in the data of Mazrouei et al. (2014), Michikami et al. (2008) and this study are -3.52 ± 0.20, -3.34 ± 0.19 and -3.05 ± 0.14, respectively. (For interpretation of the references to colour in this figure legend, the reader is referred to the web version of this article.)

their mean b'/a' ratio (0.62) resemble the data of this study.

The diagram of mean b'/a' axial ratios vs. boulders with a diameter larger than 5 m on Itokawa is plotted in Fig. 13. Fig. 13 shows that the mean b'/a' slightly tend to increase as the boulder diameter decreases.

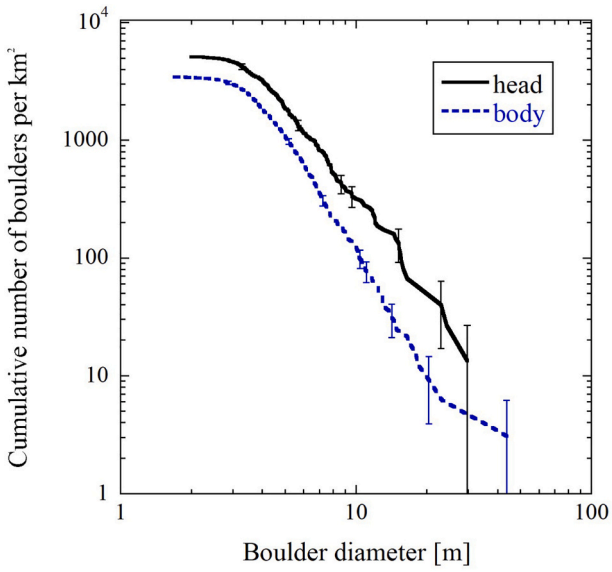

Fig. 11. Cumulative boulder size distributions per unit area on Itokawa's 'head' and 'body'. The power-indices of the boulder size distributions in the head and body are -2.62 ± 0.19 and -3.44 ± 0.22, respectively.

5. Comparison of boulders on asteroids Eros, Itokawa and Ryugu

5.1. Boulder size distributions

We compare the new boulder data from asteroids Eros and Itokawa obtained using SBMT with the boulders on Ryugu as investigated by Michikami et al. (2019). Cumulative boulder size distributions on the entire surfaces of Eros, Itokawa and Ryugu are shown in Fig. 14. Solid lines show the data obtained by the same measurer (T. Michikami). We add the Eros data by Dombard et al. (2010) to demonstrate the similarities for boulders larger than 30 m and extend the size range to the smaller sizes they measured.

Among the three asteroids of this study, the number density of boulders larger than 5 m is highest on Ryugu. In the $\geq$ 30 m range, the number density on Ryugu is about thirty times as large as on Eros (Table. 2). The difference between Itokawa and Ryugu in terms of number

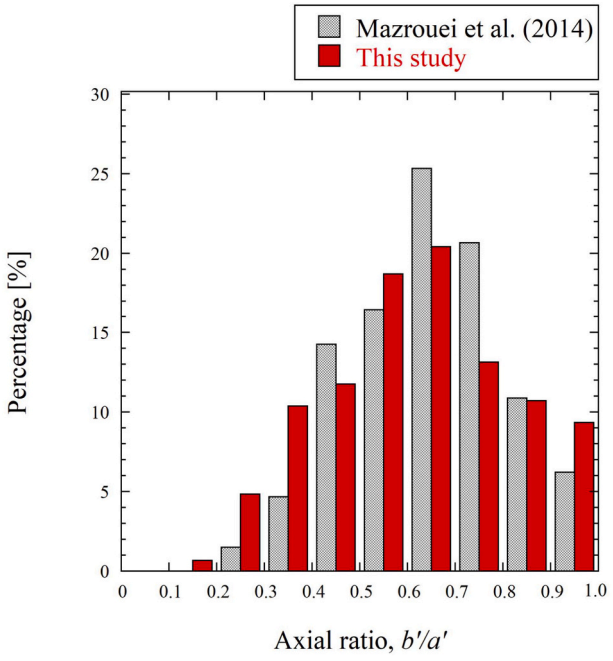

Fig. 12. Histogram of b'/a' of boulders larger than 6 m over the entire surface of Itokawa, from the data of Mazrouei et al. (2014) and this study, with the number of boulders in each bin normalized to the total number of boulders on each data set. The mean b'/a' ratios are 0.65 for Mazrouei et al. (2014) and 0.62 for this study.

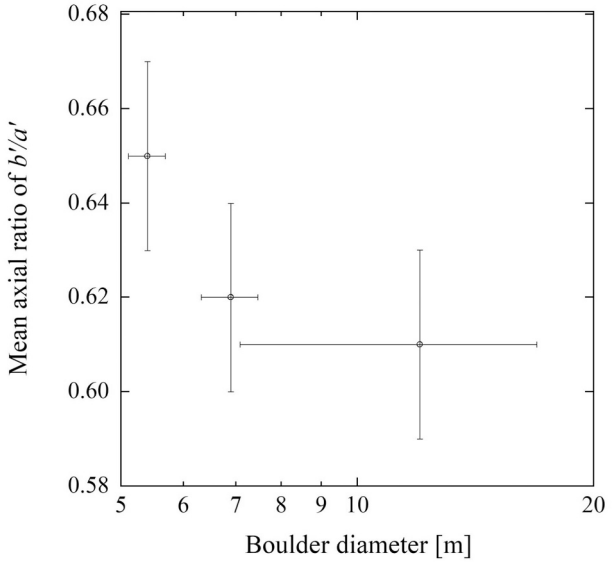

Fig. 13. Diagram of mean b'/a' ratio vs. the boulder representative diameter for the size range on Itokawa, using our data presented in Fig. 12. The boulder representative diameter is the mean diameter of boulders in each bin. The three representative diameters for the size range are 5.4 m ranging from 5 to 6 m (203 boulders), 6.9 m ranging from 6 to 8 m (181 boulders), and 12.0 m in the range larger than 8 m (108 boulders). Standard error and standard deviation of each bin are shown as vertical and horizontal bars, respectively.

density reduces as the boulder size decreases; for sizes larger than 5 m the number density on Ryugu is 1.3 times that on Itokawa. Note that the number density of boulders smaller than 10 m on Itokawa investigated by Mazrouei et al. (2014) is much larger than ours and also exceeds that on Ryugu. After all, we consider the data in Fig. 14 to be suitable for comparing the boulder size distributions on asteroids Eros, Itokawa and

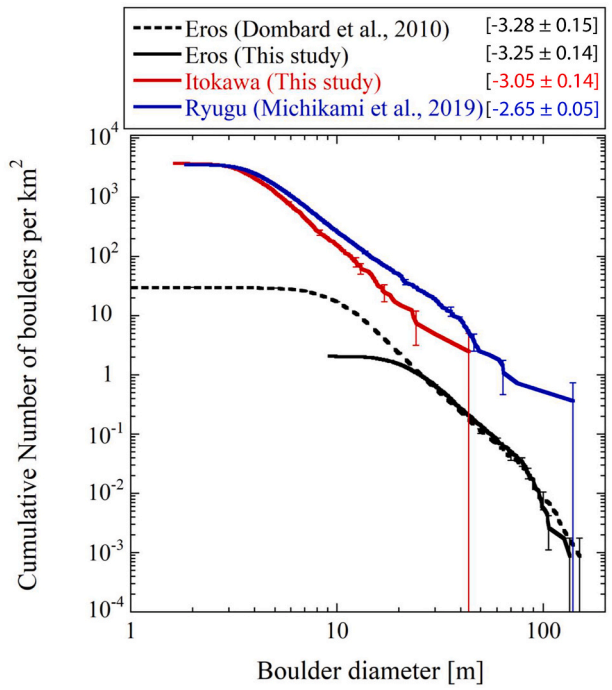

Fig. 14. Global, cumulative boulder size distributions on Eros (black dashed line: Dombard et al., 2010, black solid line: this study), Itokawa (red solid line: this study) and Ryugu (blue solid line: Michikami et al., 2019). The power-indices of these size distributions are given in square brackets. (For interpretation of the references to colour in this figure legend, the reader is referred to the web version of this article.)

Table 2
Number density of the boulders with a diameter larger than D_2 [m] per km^2.

	Eros	Itokawa	Ryugu
$D_2 \geq 30$ m	0.66	5	19
$D_2 \geq 20$ m	2.3*	15	50
$D_2 \geq 10$ m	17*	158	269
$D_2 \geq 5$ m	–	1234	1633

* Data of Dombard et al. (2010).

Ryugu because, having been taken by the same measurer, they are not affected by the observer's subjective bias.

5.2. Boulder shape distributions

Fig. 15 shows the histogram of the apparent b/a (b'/a') ratios of boulders on the entire surfaces of Eros, Itokawa and Ryugu, respectively, where the number of boulders in each bin is normalized to the total number of boulders on each asteroid. On Ryugu, the boulders located north of 60°N and south of 60°S are excluded because their shapes may not represent the real shapes owing to difficulties in making the measurements at high latitudes (Michikami et al., 2019).

The mean b'/a' ratios of boulders on Eros, Ryugu and Itokawa are 0.72, 0.68 and 0.63, respectively. This difference is statistically significant at the 99% confidence level, as shown by the Kruskal-Wallis test, which yields p-values of less than 10^{-4} for the three mean axial ratios. This suggests that mean b'/a' ratios decrease as the size of the asteroid decreases.

As mentioned before, the boulder shape distribution on Eros closely resembles laboratory impact fragments. On Itokawa, the percentage of boulders in the region of the histogram denoted by $b'/a' \leq 0.4$ is the highest among these asteroids, and as a result, the mean b'/a' ratio is the lowest. In other words, the boulders on Itokawa have more elongated

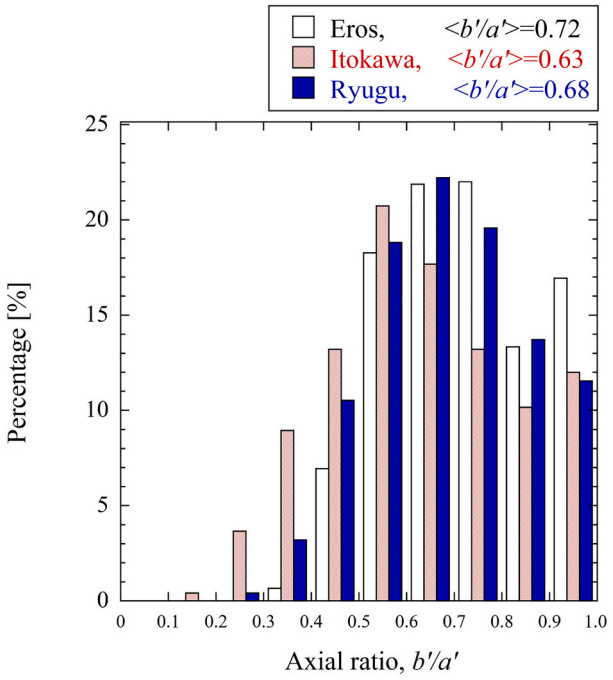

Fig. 15. Histogram of b'/a' ratios of boulders on the entire surfaces of Eros (this study), Itokawa (this study) and Ryugu (Michikami et al., 2019), with the number of boulders in each bin normalized to the total number of boulders on each asteroid. On Eros, boulders larger than 30 m are shown, with a total of 750. On Itokawa and Ryugu, boulders larger than 5 m are indicated with total numbers of 492 and 3848, respectively. The mean b'/a' ratios are indicated in angle brackets (note that, on Itokawa, the mean b'/a' for boulders larger than 5 m is slightly greater for boulders larger than 6 m shown in Fig. 12).

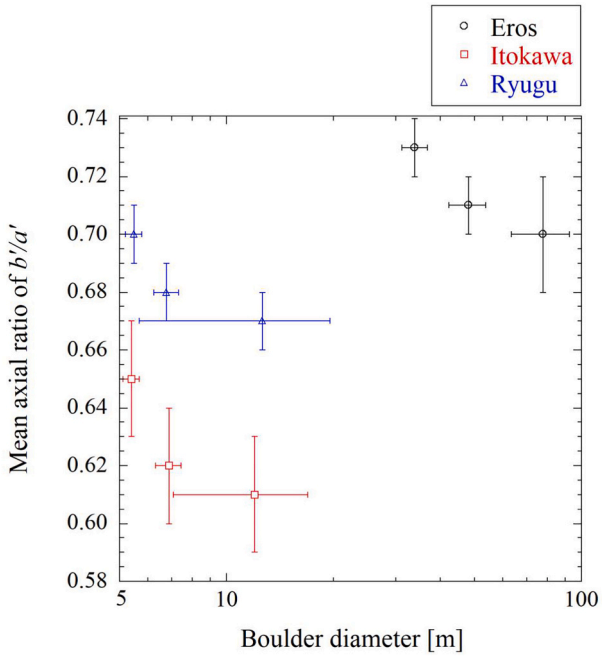

Fig. 16. Diagram of mean b'/a' ratios vs. boulder representative diameter for the size range on Eros, Itokawa and Ryugu. On Ryugu, the three representative diameters for the size range are 5.5 m ranging from 5 to 6 m (1397 boulders), 6.8 m ranging from 6 to 8 m (1354 boulders), and 12.6 m in the range larger than 8 m (1097 boulders). Standard error and standard deviation of each bin are shown as vertical and horizontal bars, respectively.

shapes compared with the boulders on Eros, Ryugu and laboratory impact fragments.

The difference in the mean b'/a' ratios may appear to be small. However, one has to bear in mind that the total range of possible values is only ~ 0.2 or so wide, so differences of 0.04 or 0.05 are very significant. In laboratory impact fragments produced by the catastrophic disruption, the mean b/a and c/a ratios are ~0.7 and ~0.5, respectively. If half of the boulders are rotated around the a axis this results in $b' = c$ and apparent $c' = b$. Consequently, the mean b'/a' becomes 0.6. Therefore, even if the orientation of a large proportion of boulders is changed as above, the resulting variation in terms of absolute mean b'/a' will remain small.

Boulder shapes are largely size-dependent. The diagrams of the mean b/a axial ratios vs. boulders with a diameter larger than 5 m on Itokawa and Ryugu, and larger than 30 m on Eros, are plotted in Fig. 16. For each asteroid, the mean b'/a' ratio tends to increase slightly as the boulder diameter decreases.

6. Discussion

6.1. Boulders – a global perspective

The power-index of the global boulder size distribution is steeper on Eros than it is on Itokawa and Ryugu. Large amounts of small particles cover Eros' surface and Eros has a lower number density of boulders than Itokawa and Ryugu. Previous studies show that most boulders on Eros originate from 7.6 km wide Shoemaker crater (e.g. Thomas et al., 2001). On the other hand, most boulders on Itokawa and Ryugu are the product of the reaccumulation of small fragments produced by the catastrophic disruption of a larger parent body (e.g. Fujiwara et al., 2006; Saito et al., 2006; Sugita et al., 2019; Michikami et al., 2019).

Itokawa's boulder size distribution has a steeper power-index than Ryugu's (Fig. 14). Because a steeper power-index is generally indicative of a higher degree of fragmentation (Hartmann, 1969; Thomas et al., 2001), the boulders accumulated on the surface of Itokawa could have been produced by a somewhat more severe disruption of Itokawa's parent body compared with Ryugu. However, it is possible that, after the formation of the asteroid, the global boulder size distribution on Itokawa became steeper due to repeated impacts and/or thermal fatigue (e.g. Delbo et al., 2014), producing more fine particles. The minimum particle size on Itokawa appears to be smaller than on Ryugu. The smooth terrains on Itokawa are likely to consist of these fine particles, while no similar smooth terrains exist on Ryugu. In fact, particles ~1 mm in size are abundant in close-up images on the surface of Itokawa (Yano et al., 2006) and Eros (Veverka et al., 2001), whereas they are not found on Ryugu (Sugita et al., 2019; Watanabe et al., 2019).

The number density of boulders decreases from Ryugu, to Itokawa and to Eros. As fragmentation by repeated impacts and/or thermal fatigue results in the reduction of the number density of boulders, Ryugu's global boulder size distribution might have been less affected by repeated impacts and/or thermal fatigue than Eros' and Itokawa's.

Michikami et al. (2010 and 2019) hypothesize that the actual shape distribution of boulders on any asteroid is similar to laboratory impact fragments, based on three lines of observational evidence: (i) over several orders of magnitude, the shapes of laboratory impact fragments produced by a catastrophic disruption have been found to behave similarly, independent of various experimental conditions and target materials; (ii) the mean b'/a' and c'/a' ratios of boulders on Itokawa and Ryugu (admittedly limited to only a very small sample) are similar to laboratory impact fragments; and (iii) the shapes of small asteroids considered to be monolithic bodies are similar to laboratory impact fragments (Michikami et al., 2010). As a theoretical interpretation for this hypothesis, Kadono et al. (2018) propose that smaller impact fragments originate from fractal crack bifurcation of a target and as a result they have a similar shape distribution, independent of experimental conditions. Kadono et al. (2018) suggest that the physics controlling the

Table 3
Properties of the three asteroids investigated in this study.

	Eros	Ryugu	Itokawa
Dimension [km]	$34 \times 11 \times 11$[a]	$1.04 \times 1.02 \times 0.88$[d]	$0.535 \times 0.294 \times 0.209$[e]
Mean diameter* [km]	16	0.98	0.32
Mass [kg]	$(6.687 \pm 0.003) \times 10^{15}$[b]	$(4.50 \pm 0.06) \times 10^{11}$[d]	$(3.510 \pm 0.105) \times 10^{10}$[e]
Mean density [kg/m^3]	2670 ± 30[b]	1190 ± 20[d]	1950 ± 14[f]
Surface gravity [m/s^2]	2.5×10^{-3} to 5.5×10^{-3}[c]	1.1×10^{-4} to 1.5×10^{-4}[d]	6.1×10^{-5} to 9.1×10^{-5}[g]

[a] Veverka et al. (2000).
[b] Yeomans et al. (2000).
[c] Zuber et al. (2000).
[d] Watanabe et al. (2019).
[e] Fujiwara et al. (2006).
[f] Abe et al. (2006).
[g] Tancredi et al. (2015).
* Geometric mean.

fragmentation processes is the same even though size may vary by several orders of magnitude.

However, the shape distributions of boulders on Eros, Ryugu and Itokawa differ slightly. Assuming that their actual boulder shape distributions should actually all be similar to laboratory impact fragments, we need to explain the difference in apparent mean b/a (b'/a') ratios of boulders between the three asteroids. At this point, it should be noted that we confirmed shapes to have little effect on boulder size distributions because mean b'/a' ratios for all asteroids are similar to laboratory impact fragments. We think that the mean b'/a' of boulders depends on the gravity of an asteroid and boulders' friction angles because those are the two main factors affecting a boulder's preferred orientation. In the case of Eros, most boulders' c axes end up perpendicular to the asteroid surface owing to the relatively high gravity. Thus, apparent and actual b/a ratios of the boulders are similar (0.72) on Eros and close to the typical value for laboratory impact fragments (~0.7). On Itokawa on the other hand, the relatively low gravity does not force that many boulders to lie down with their c axes perpendicular to the asteroid surface. This provides an explanation for the deviation of apparent b/a ratios from actual b/a ratios, and thereby the apparent mean b/a ratio (0.63) on Itokawa, which is lower than the ~0.7 ratio observed in laboratory impact fragments. In terms of gravity, Ryugu falls between the two and so, at 0.68, the mean b'/a' ratio lies between Eros' and Itokawa's, as expected.

Fig. 16 shows that the mean b'/a' ratio of the boulders tends to slightly increase as the boulder diameter decreases. In general, particles smaller in size have higher mobility due to their lower friction angle, whereas larger boulders cannot move that easily and some boulders get stuck at the surface owing to their larger friction angle (e.g. Miyamoto et al., 2007; Michikami et al., 2010, 2019). Thus, as small boulders' c axes tend to be perpendicular to the asteroid surface owing to their low friction angles, their mean b'/a' ratios can be expected to increase with decreasing size.

6.2. Boulders – a local perspective

According to Brack and McMahon (2019), the dynamical mechanism of boulder motion is influenced by many factors. These include regolith grain size and composition, the existence of other boulders in the movement path, the cohesive forces between boulder and regolith, and the shape of the moving boulder (Brack and McMahon, 2019). Our comparisons of the global data of boulders on the asteroids Eros, Itokawa and Ryugu suggest that it is mainly gravity and/or boulder size that affects boulder migration. In addition, size sorting and vertical migration due to the seismic shaking produced by recurring impacts is probably also largely affected by gravity.

For each asteroid, it is important to investigate the boulder size and shape distributions on a local scale, within regions of different gravities, in order to understand the migration of boulders. This is because the migration of boulders may change boulder size and shape distributions on local scales due to different local gravities. For instance, Tancredi et al. (2015) studied the boulder size and shape distributions within regions of Itokawa in detail and indicated that their size distributions are correlated with surface gravity. We want to progress one step further towards understanding a correlation between gravity and boulder size and shape and investigate the data on local scales for regions with different gravities for each asteroid next. We have listed the basic properties including the surface gravities for Eros, Itokawa and Ryugu in Table. 3.

For each asteroid, we make an arbitrary selection from a high and a low gravitational potential region (Figs. 17 and 18). In general, the direction of migration of boulders is considered to be from high to low gravitational potential regions. On Eros and Itokawa, the high and the low gravitational potential regions correspond to low and high gravities, respectively, while the reverse is currently true on Ryugu. In the case of Ryugu, at a some point in its past, Ryugu rotated much faster, the resultant strong centrifugal force causing mass movement towards the equator (e.g. Watanabe et al., 2019; Sugita et al., 2019; Michikami et al., 2019). At present, the equatorial region has slightly lower gravitational potential and low gravity compared with the high latitudes (e.g. Sugita et al., 2019).

Note that if the relationship between surface gravity and boulder migration to be quantitatively investigated, more information other than just gravity would be necessary as mentioned above. We consider any more complex modelling to be beyond the scope of this study and limit ourselves to providing what we consider to be an essential first step towards a better understanding of the local differences in boulder size and shape distributions within regions of different gravities.

Fig. 17 shows the boulder size distributions including the two regions with different gravitational potential on Eros, Itokawa and Ryugu. On Eros, the local number densities of the boulders in both regions shown in Fig. 17 are lower than the global surface average. This is probably because both regions selected are relatively distant from Shoemaker crater, and nearly half of all boulders can be found within Shoemaker crater (Thomas et al., 2001). On Ryugu and Itokawa, the number densities of boulders are higher in the high gravitational potential regions than they are globally, while the reverse is true for boulders in regions of low gravitational potential.

The power-indices of the boulder size distributions do not vary drastically between high and low gravitational potential regions. The p-values of the Wilcoxon rank sum test between the high and low gravitational potential regions are 0.17 for Eros, 0.12 for Itokawa and 0.29 for Ryugu, suggesting a 95% confidence level that the differences are not statistically significant. We note that the power-indices of the boulder size distributions on Itokawa and Ryugu are slightly steeper at low than they are at high gravitational potentials. This tendency on Itokawa and Ryugu corresponds with Tancredi et al.'s (2015) observation that a steeper size distribution correlates with low gravitational potential,

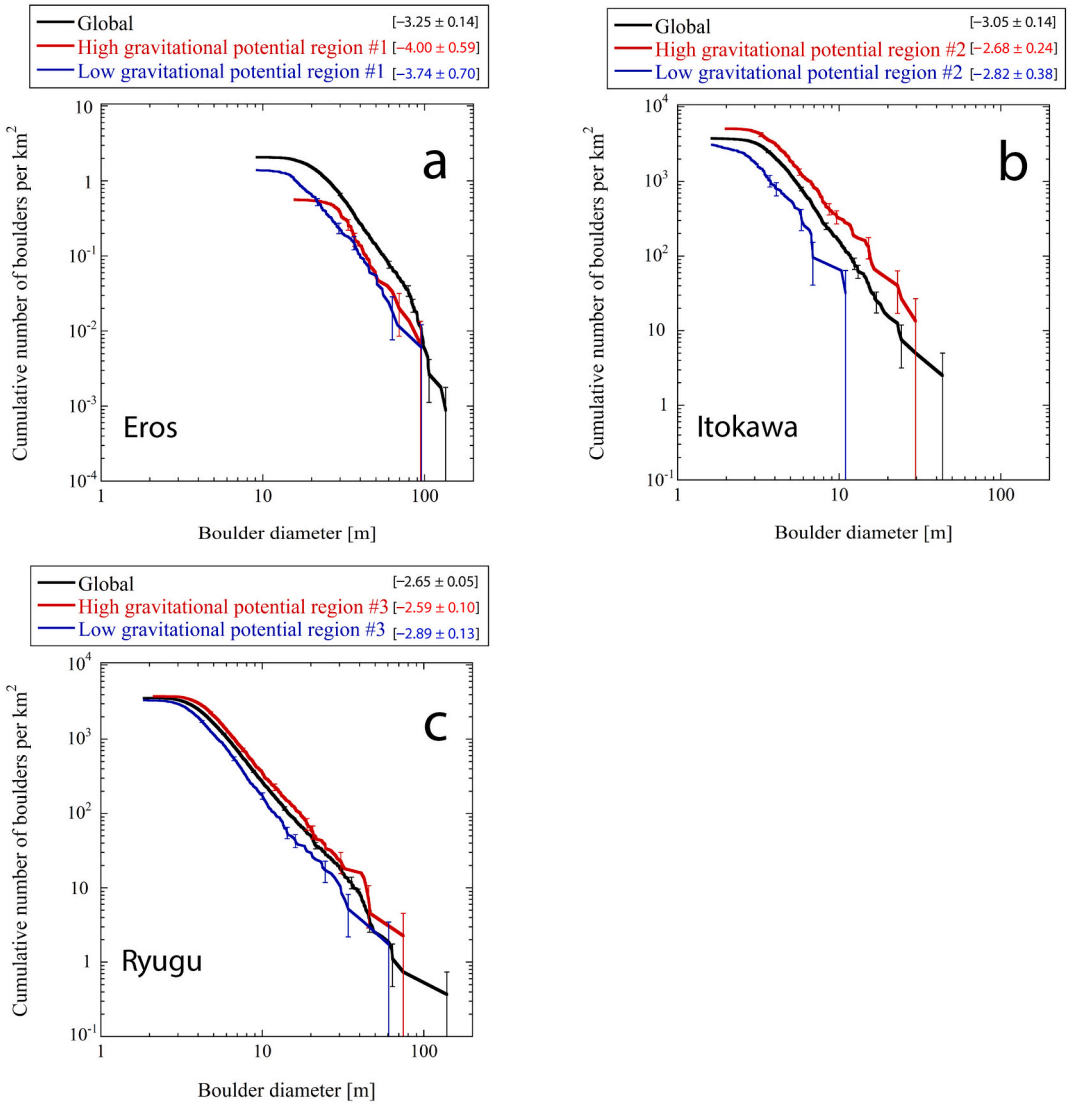

Fig. 17. Cumulative boulder size distributions in the high and low gravitational potential regions added to the global data for each asteroid. The high gravitational potential regions of #1, #2 and #3 are an edge (30°S – 30°N and 320° – 360°E) of Eros, the head of Itokawa, and the north (40°N – 90°N and 0° – 360°E) of Ryugu, respectively. The low gravitational potential regions of #1, #2 and #3 are the north (30°N – 90°N and 0° – 360°E) of Eros, the Sagamihara smooth area of Itokawa, and the low latitude (10°S – 10°N and 0° – 360°E) of Ryugu, respectively. The power-indices of these size distributions are given in square brackets.

which is caused by the small boulders moving towards areas of high surface gravity in the past. Thus, the slightly steeper size distribution of the boulders at a low gravitational potential implies the migration of preferentially small boulders.

Boulder shape distributions including the two different gravitational potential regions on Eros, Itokawa and Ryugu are shown in Fig. 18. On Eros, there is little difference between the boulder shape distributions in the high and the low gravitational potential regions, and shape distributions resemble laboratory impact fragment distributions. The *p*-value of the Wilcoxon rank sum test between the high and low gravitational potential regions is 0.25, suggesting a 95% confidence level that the difference is not statistically significant. This result supports the hypothesis that almost all boulders on Eros have been re-orientated after their accumulation by global vibrations (e.g. Richardson et al., 2005) and consequently the *c* axes of most boulders can be expected to be orientated perpendicular to the surface (Michikami et al., 2019).

On Itokawa and Ryugu on the other hand, the mean b'/a' ratios are larger in the low gravitational potential regions than at high gravitational potential. The *p*-values of the Wilcoxon rank sum test between the high and low gravitational potential regions on Itokawa and Ryugu are 0.02 and less than 10^{-4}, respectively, suggesting statistical significance of the difference at a 95% and a 99% confidence level. In particular, the mean b'/a' ratios in the low gravitational potential regions on Itokawa and Ryugu are 0.71 and 0.70, respectively, which is similar to laboratory impact fragments. This is considered to be the product of migration from another area and/or the subsurface, and as a result the *c* axes of most boulders become aligned perpendicular to the surface due to gravitational stability (e.g. Michikami et al., 2019).

In this investigation of the boulders on Itokawa and Ryugu, the more rounded boulders are found in the low gravitational potential regions. This appears to contradict the trend presented by Tancredi et al. (2015) who suggested that more rounded boulders are found in the high gravitational potential of Itokawa. However, even in the high gravitational potential region of Itokawa, we find a b'/a' ratio of 0.65 in our observations, which is still slightly larger than that the global value, 0.63. In this sense, there is no disagreement between our observations and Tancredi et al.'s (2015) results.

The cause of the relatively small global value of b'/a' ratio may be related to Itokawa's "sea otter" shape, i.e. its comparatively smaller, rather round head and larger oval body (Fujiwara et al., 2006).

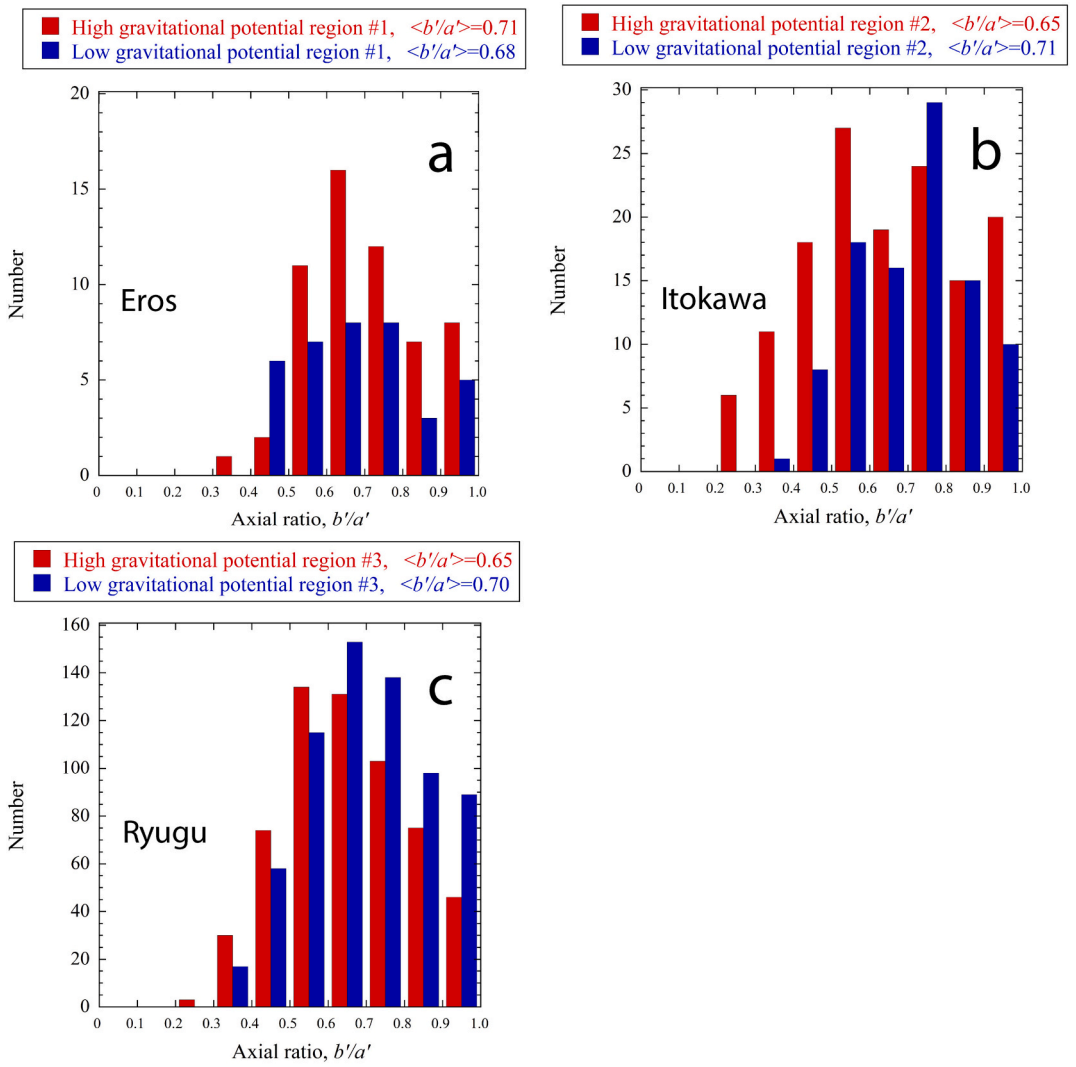

Fig. 18. Histogram of b'/a' ratios of boulders in the high and low gravitational potential regions for each asteroid. On Eros, boulders larger than 30 m are shown. On Itokawa, boulders larger than 5 m and 1.6 m are shown in the high and low elevation regions #2, respectively. On Ryugu, boulders larger than 5 m are shown, with only the data of 40°N – 60°N and 0° – 360°E used in the high gravitational potential region #3. The mean b'/a' ratios are given in angle brackets. The histograms correspond to the size distributions in Fig. 17 a, b and c, respectively.

According to Mazrouei et al. (2014), the most likely scenario for the formation of Itokawa is that the parent body of Itokawa underwent disruption through a collision with another object, and the largest two fragments made up the head and body of current Itokawa. There is a possibility that the enhanced population of boulders along the equator of the body reflects a size and shape distribution largely unchanged since Itokawa's formation. That is, many large boulders at the equator became stranded at the surface and remain at their original orientations. In fact, in our data, the mean b'/a' ratio of the boulders larger than 5 m near the equator (from 20°S to 20°N) of the body of Itokawa is small, 0.60. It is this low b'/a' ratio which affects the global value significantly, giving the impression of a global population of more elongated boulders.

After all, although a more detailed investigation into the relationship between local surface gravity and boulder migration will be needed in the future, it is safe to say that local size and shape distributions in regions with extremely different gravities also indicate that boulder migration tends to preferentially affect smaller boulders and low gravitational potential regions. Even though these ideas were already outlined by Michikami et al. (2010) and Michikami et al. (2019), this study goes much further in providing the first coherent set of quantitative data on boulder size distributions on three different asteroids, presenting a robust body of evidence for this conceptual model of boulder formation and movement on asteroid surfaces.

7. Conclusion

We investigated the boulder sizes and shapes on three asteroids with different global and local gravity regimes. First, we tried to establish a consistent and coherent way of comparing size distributions of boulders and/or fragments. The relationships between the sphere-equivalent diameter, D_s (which reflects the real volume of the fragment) and descriptors of fragment size $D_1 - D_5$ were investigated using measurements taken on laboratory impact fragments in basalt. Our results show that the fragment size D_5 is closest to the sphere-equivalent diameter, D_s in terms of the size distribution. Regarding actual observations of boulders on asteroids, we think that the fragment size D_2 is a suitable proxy for reflecting the real volume of a boulder as it does not require knowledge of the boulder's c axis. The sphere-equivalent diameter, D_s can then be approximated as $0.65 \times D_2$. We found that the sum of individual fragment volumes using $0.65 \times D_2$ is almost identical to the total volume of fragments as determined by weight. In this study, we therefore adopted D_2 as the definition of a boulder's size.

We approximated the outlines of boulders as ellipses, and then the long and short axes of boulders on Eros and Itokawa were measured

using SBMT. On Eros, we focused on boulders larger than 30 m because of limited image resolution. More than 2300 boulders $\geq$ 9 m were measured and nearly 750 boulders $\geq$ 30 m were identified using SBMT. At diameters $\geq$ 30 m, the boulder size distribution on Eros in this study is roughly the same as Dombard et al.'s (2010). On Itokawa, available image resolution required a focus on boulders larger than 5 m. Nearly 1500 boulders $\geq$ 1.6 m were measured and nearly 490 boulders $\geq$ 5 m were identified using SBMT. The global and regional, 'head and body' boulder size distributions of Itokawa are compatible with the data of Michikami et al. (2008) and Tancredi et al. (2015), who used DS9. However, we found a different boulder size distribution from Mazrouei et al. (2014) for Itokawa, especially in terms of number density of the boulders, despite using the same tool, SBMT. A possible explanation is that Mazrouei et al. (2014) might have used lower resolution images than we did.

We compared our new boulder data for asteroids Eros and Itokawa obtained using SBMT with the boulder data for Ryugu reported by Michikami et al. (2019). At diameters $\geq$ 5 m, the number density on Ryugu is the highest among these asteroids. As for boulders larger than 30 m, their number density on Ryugu is about thirty times larger than on Eros. The power-indices of the boulder size distributions are -3.25 ± 0.14 for Eros, -3.05 ± 0.14 for Itokawa and -2.65 ± 0.05 for Ryugu.

The shape distributions of the boulders on the three asteroids differ. Their apparent mean b/a ratios are 0.72 for Eros, 0.68 for Ryugu and 0.63 for Itokawa, indicating that the apparent mean b/a decreases with asteroid size. Moreover, the apparent mean b/a ratios of individual boulders tend to slightly increase as the boulder diameter decreases. Assuming that the actual shape distribution of boulders on any asteroid is similar to laboratory impact fragments, the apparent mean b/a ratios indicate a preferred orientation of the boulders which is largely affected by two factors: the gravity on an asteroid and the boulders' friction angles. The local shape distributions of boulders between regions with different gravities for each asteroid also support this hypothesis. In conclusion, migration of boulders tends to play a more significant role for smaller boulders, and on larger asteroids.

Declaration of Competing Interest

None.

Acknowledgements

The authors would like to thank all members of Hayabusa2 mission team for their support of the data acquisition of Ryugu. We acknowledge Dr. C. M. Ernst for supporting of SBMT and Dr. P. C. Thomas for providing data of Eros. We are very grateful for Dr. S. Mazrouei's and Dr. O.S. Barnouin's assistance by providing data of Itokawa. Mr. Y. Hashimoto and Dr. H. Kikuchi supported the measurements. We thank Dr. S. Hasegawa for useful discussions. We also thank Professor G. Tancredi and an anonymous referee for their careful review of the manuscript and their constructive comments. This study was partly supported by the JSPS KAKENHI Grant Number 20K04048 for TM and by the Hypervelocity Impact Facility, ISAS, JAXA.

Appendix A. Data from laboratory impact experiments into basalt

All samples in this study are fragments of basalt targets, obtained in earlier laboratory impact experiments by Michikami et al. (2016). The sample material from Linxi, Inner Mongolia is relatively coarse-grained basalt with very homogeneous texture on a scale of ~1 mm. Target bulk density is 3000 kg/m^3, compressive strength is 185 MPa, and tensile strength is 14 MPa. The compressional wave velocity is 6.1 km/s, measured using a pulse transition method for a slab sample 1 cm in thickness.

The impact experiments were carried out with a two-stage light-gas gun at the Institute of Space and Astronautical Science, Japan Aerospace Exploration Agency (ISAS, JAXA). A total of 23 impact experiments were performed by firing a spherical nylon projectile (diameter 7.14 mm, mass 0.217 g and density 1140 kg/m^3) perpendicularly into cubic targets with 5 to 15 cm side length at velocities of 1.60 to 7.13 km/s. In all runs, the projectiles hit the center of the targets.

Each target was set on a cylindrical stand less than one third of the target size in diameter. The whole system was mounted in a vacuum chamber (almost $1 \times 1 \times 2$ m^3) with acrylic resin windows. The ambient pressure in the chamber was less than 200 Pa. To prevent the destruction of fragments by secondary collisions with the interior chamber, the interior was clad with several styrofoam boards or urethane sheets. After the impact, we collected all fragments in the chamber. The three axes, a, b, c and individual masses of more than 12,700 fragments with $b \geq 4$ mm generated in the impact experiments were measured by Michikami et al. (2016). In this study, we investigate the relationship between a fragment's size and its volume using these same fragments. For a more detailed description of the experiments, see Michikami et al. (2016).

References

Abe, S., Mukai, T., Hirata, N., et al., 2006. Mass and local topography measurements of Itokawa by Hayabusa. Science 312, 1344–1347.
Brack, D.N., McMahon, J.W., 2019. Modeling the coupled dynamics of an asteroid with surface boulder motion. Icarus 333, 96–112.
Capaccioni, F., Cerroni, P., Coradini, M., et al., 1984. Shapes of asteroids compared with fragments from hypervelocity impact experiments. Nature 308, 832–834.
Capaccioni, F., Cerroni, P., Coradini, M., et al., 1986. Asteroidal catastrophic collisions simulated by hypervelocity impact experiments. Icarus 66, 487–514.
Chapman, C.R., Merline, W.J., Thomas, P.C., et al., 2002. Impact history of Eros: craters and boulders. Icarus 155, 104–118.
Clauset, A., Shalizi, C.R., Newman, M.E.J., 2009. Power-law distributions in empirical data. SIAM Rev. 51, 661–703.
Delbo, M., Libourel, G., Wilkerson, J., et al., 2014. Thermal fatigue as the origin of regolith on small asteroids. Nature 508, 233–236. https://doi.org/10.1038/nature13153.
DeSouza, I., Daly, M.G., Barnouin, O.S., et al., 2015. Improved techniques for size-frequency distribution analysis in the planetary sciences: application to blocks on 25143 Itokawa. Icarus 247, 77–80.
Dombard, A.J., Barnouin, O.S., Prockter, L.M., Thomas, P.C., 2010. Boulders and ponds on the asteroid 433 Eros. Icarus 210, 713–721.
Durda, D.D., Bagatin, A.C., Aleman, R.A., et al., 2015. The shapes of fragments from catastrophic disruption events: effects of target shape and impact speed. Planet. Space Sci. 107, 77–83.
Ernst, C.M., Barnouin, O.S., Daly, R.T., the Small Body Mapping Tool Team, 2018. The small body mapping tool (SBMT) for accessing visualizing, and analyzing spacecraft data in three dimensions. Lunar Planet. Sci. Conf. 49 (2083).
Fujiwara, A., Kamimoto, G., Tsukamoto, A., 1978. Expected shape distribution of asteroids obtained from laboratory impact experiments. Nature 272, 602–603.
Fujiwara, A., Kawaguchi, J., Yeomans, D.K., et al., 2006. The rubble-pile asteroid Itokawa as observed by Hayabusa. Science 312, 1330–1334.
Grott, M., Biele, J., Michel, P., et al., 2020. Macroporosity and grain density of rubble pile asteroid (162173) Ryugu. J. Geophys. Res. Planets. 125, e2020JE006519 https://doi.org/10.1029/2020JE006519.
Hartmann, W.K., 1969. Terrestrial, lunar, and interplanetary rock fragmentation. Icarus 10, 201–213.
Kadono, T., Tanigawa, T., Kurosawa, K., et al., 2018. Correlation between fragment shape and mass distributions in impact disruption. Icarus 309, 260–264.
Lauretta, D.S., DellaGiustina, D.N., Bennett, C.A., et al., 2019. The unexpected surface of asteroid (101955) Bennu. Nature 568, 55–60. https://doi.org/10.1038/s41586-019-1033-6.
Mazrouei, S., Daly, M.G., Barnouin, O.S., et al., 2014. Block distribution on Itokawa. Icarus 229, 181–189.
Michikami, T., Nakamura, A.M., Hirata, N., et al., 2008. Size-frequency statistics of boulders on global surface of asteroid 25143 Itokawa. Earth Planets Space 60, 13–20.
Michikami, T., Nakamura, A.M., Hirata, N., 2010. The shape distribution of boulders on asteroid 25143 Itokawa: comparison with fragments from impact experiments. Icarus 207, 277–284.
Michikami, T., Hagermann, A., Kadokawa, T., et al., 2016. Fragment shapes in impact experiments ranging from cratering to catastrophic disruption. Icarus 264, 316–330.
Michikami, T., Kadokawa, T., Tsuchiyama, A., et al., 2018. Influence of petrographic textures on the shapes of impact experiment fine fragments measuring several tens of microns: comparison with Itokawa regolith particles. Icarus 302, 109–125.
Michikami, T., Honda, C., Miyamoto, H., et al., 2019. Boulder size and shape distributions on asteroid Ryugu. Icarus 331, 179–191.
Miyamoto, H., Yano, H., Scheeres, D.J., et al., 2007. Regolith migration and sorting on asteroid Itokawa. Science 316, 1011–1014.

Nakamura, A.M., Michikami, T., Hirata, N., et al., 2008. Impact process of boulders on the surface of asteroid 25143 Itokawa—fragments from collisional disruption. Earth Planets Space 60, 7–12.
Pajola, M., Bierhaus, B., Walsh, K.J., et al., 2019. Surface densities and size-frequency distributions of meter-size boulders inside craters on (101955) Bennu. In: American Geophysical Union, Fall Meeting 2019, abstract #P53C-3456.
Richardson, J.E., Melosh, H.J., Greenberg, R.J., et al., 2005. The global effects of impact-induced seismic activity on fractured asteroid surface morphology. Icarus 179, 325–349.
Saito, J., Miyamoto, H., Nakamura, R., et al., 2006. Detailed images of asteroid 25143 Itokawa from Hayabusa. Science 312, 1341–1344.
Schwartz, S., Ballouz, R.L., Asphaug, E., et al., 2019. The global distribution of boulder orientations on (101955) Bennu. In: EPSC-DPS Joint Meeting 2019 id. EPSC-DPS2019-1139.
Sugita, S., Honda, R., Morota, T., et al., 2019. The geomorphology, color, and thermal properties of Ryugu: implications for parent-body processes. Science 364. https://doi.org/10.1126/science.aaw0422.
Tancredi, G., Roland, S., Bruzzone, S., 2015. Distribution of boulders and the gravity potential on asteroid Itokawa. Icarus 247, 279–290.
Thomas, P.C., Veverka, J., Robinson, M.S., Murchie, S., 2001. Shoemaker crater as the source of most ejecta blocks on the asteroid 433 Eros. Nature 413, 394–396.
Veverka, J., Robinson, M., Thomas, P., et al., 2000. NEAR at Eros: imaging and spectral results. Science 289, 2088–2097.
Veverka, J., Farquhar, B., Robinson, M., et al., 2001. The landing of the NEAR-Shoemaker spacecraft on asteroid 433 Eros. Nature 413, 390–393.
Walsh, K.J., Jawin, E.R., Ballouz, R.-L., et al., 2019. Craters, boulders and regolith of (101955) Bennu indicative of an old and dynamic surface. Nat. Geosci. 12, 242–246. https://doi.org/10.1038/s41561-019-0326-6.
Watanabe, S., Hirabayashi, M., Hirata, N., et al., 2019. Hayabusa2 arrives at the carbonaceous asteroid 162173 Ryugu—a spinning top–shaped rubble pile. Science 364, 268–272. https://doi.org/10.1126/science.aav8032.
Yano, H., Kubota, T., Miyamoto, H., et al., 2006. Touchdown of the Hayabusa spacecraft at the Muses Sea on Itokawa. Science 312, 1350–1353.
Yeomans, D.K., Antreasian, P.G., Barriot, J.-P., et al., 2000. Radio science results during the NEAR-Shoemaker spacecraft rendezvous with Eros. Science 289, 2085–2088.
Zuber, M.T., Smith, D.E., Cheng, A.F., et al., 2000. The shape of 433 Eros from the NEAR-Shoemaker laser rangefinder. Science 289, 2097–2101.